

Binder free and flexible asymmetric supercapacitor exploiting Mn<sub>3</sub>O<sub>4</sub> and MoS<sub>2</sub> nanoflakes on carbon fibers

*Original*

Binder free and flexible asymmetric supercapacitor exploiting Mn<sub>3</sub>O<sub>4</sub> and MoS<sub>2</sub> nanoflakes on carbon fibers / Rafique, A.; Zubair, U.; Serrapede, M.; Fontana, M.; Bianco, S.; Rivolo, P.; Pirri, C. F.; Lamberti, A.. - In: NANOMATERIALS. - ISSN 2079-4991. - 10:6(2020), p. 1084. [10.3390/nano10061084]

*Availability:*

This version is available at: 11583/2836583 since: 2020-06-19T12:48:56Z

*Publisher:*

MDPI AG

*Published*

DOI:10.3390/nano10061084

*Terms of use:*

This article is made available under terms and conditions as specified in the corresponding bibliographic description in the repository

*Publisher copyright*

(Article begins on next page)



# Binder Free and Flexible Asymmetric Supercapacitor Exploiting $\text{Mn}_3\text{O}_4$ and $\text{MoS}_2$ Nanoflakes on Carbon Fibers

Amjid Rafique <sup>1,\*</sup>, Usman Zubair <sup>1,2</sup>, Mara Serrapede <sup>3</sup>, Marco Fontana <sup>3</sup>, Stefano Bianco <sup>1</sup>, Paola Rivolo <sup>1</sup>, Candido F. Pirri <sup>1,3</sup> and Andrea Lamberti <sup>1,3,\*</sup>

<sup>1</sup> Politecnico di Torino, Dipartimento di Scienza Applicata e Tecnologia (DISAT), Corso Duca Degli Abruzzi, 24, 10129 Turin, Italy; usman.zubair@polito.it (U.Z.); stefano.bianco@polito.it (S.B.); paola.rivolo@polito.it (P.R.); fabrizio.pirri@polito.it (C.F.P.)

<sup>2</sup> Faculty of Engineering and Technology, National Textile University, Faisalabad 38000, Pakistan

<sup>3</sup> Istituto Italiano di Tecnologia, Center for Sustainable Future Technologies, Corso Trento, 21, 10129 Turin, Italy; mara.serrapede@iit.it (M.S.); marco.fontana@iit.it (M.F.)

\* Correspondence: amjid.rafique@polito.it (A.R.); andrea.lamberti@polito.it (A.L.)

Received: 30 April 2020; Accepted: 26 May 2020; Published: 31 May 2020

**Abstract:** Emerging technologies, such as portable electronics, have had a huge impact on societal norms, such as access to real time information. To perform these tasks, portable electronic devices need more and more accessories for the processing and dispensation of the data, resulting in higher demand for energy and power. To overcome this problem, a low cost high-performing flexible fiber shaped asymmetric supercapacitor was fabricated, exploiting 3D-spinel manganese oxide  $\text{Mn}_3\text{O}_4$  as cathode and 2D molybdenum disulfide  $\text{MoS}_2$  as anode. These asymmetric supercapacitors with stretched operating voltage window of 1.8 V exhibit high specific capacitance and energy density, good rate capability and cyclic stability after 3000 cycles, with a capacitance retention of more than 80%. This device has also shown an excellent bending stability at different bending conditions.

**Keywords:** supercapacitors;  $\text{Mn}_3\text{O}_4$ ;  $\text{MoS}_2$ ; fiber-shaped; flexible

## 1. Introduction

In very recent years, supercapacitors (SCs) have gained a considerable attention, because of their ability to deliver higher power density than batteries, and to store higher energy density than electrostatic capacitors [1,2]. To bridge the gap of energy density between batteries and conventional capacitors, supercapacitors have been used in a variety of applications, ranging from portable electronic devices, hybrid electrical vehicles and large industrial scale power and energy management [3,4].

The behavior of SCs is strongly influenced by the layout, sealing and packaging technology, the separator, the electrolyte, the current collectors and, most importantly, it is influenced by the active materials at the electrodes [5]. For this reason, it is essential to develop new materials and new structures able to deliver high specific capacitance, and to sustain high cycling stability with a good rate capability. Based on the charge storage mechanism, SCs are classified as electrical double layer capacitors (EDLCs) and pseudocapacitors. The EDLCs are characterized by extremely large surface area achieved by a good compromise between open pores, size of the pores and dimension of the charges in the electrolyte that generate the double-layer region with the electrode surface. Usually carbon-based materials give rise to large values of EDL capacitance. Together with this phenomenon, a large group of metal oxides, transition metal dichalcogenides, carbides and

conducting polymers exhibit pseudocapacitance that is generated by fast and reversible Faradaic reactions occurring at the electrode/electrolyte interface, or in the bulk very close to the electrode surface. Pseudocapacitors show higher capacitance when compared to EDLC-based devices, but they usually have a limited cyclic life, due to the degradation of the active material upon continuous redox reactions. Even though the two phenomena are intrinsically different, they can be grouped because of their intrinsic kinetics, allowing to systematically study the charge storage mechanisms in hybrid electrodes and differentiate capacitive-controlled and diffusion-controlled charge storage mechanisms [6]. The challenge of the current SCs is to increase the energy density without sacrificing power density and cyclic life [7]. According to the equation which describes the energy stored in a capacitor:

$$E = 1/2CV^2$$

where C is the capacitance and V the voltage, there are two possibilities to enhance the energy density of the device: (i) by increasing the specific capacitance of the device, (ii) by increasing the operating potential window. The main limitation to the increase of the voltage window is the stability of the electrolyte, especially when working with aqueous-based solutions, due to the electrolysis of water. This limitation occurs also in the water-based gel-polymer electrolytes, greatly required to realize portable and wearable supercapacitors [8].

The development of asymmetric supercapacitors in which the anode and cathode are clearly distinct is a good approach to improve their energy density, because the combination of appropriate electrode materials with complementary potential windows allows to enlarge the operating voltage of the device [9,10]. Carbon-based materials are usually exploited as anode, while pseudocapacitive materials, such as oxides, are usually set at the cathode. Together with carbon-based materials, transition metal dichalcogenides ( $WS_2$  [11,12],  $Bi_2S_3$  [13,14],  $Bi_2Te_3$  [15],  $MoSe_2$  [16,17],  $MoTe_2$  [18,19],  $ZnS$  [20,21],  $FeS_2$  [22]) can be used as an anode, thanks to their intrinsic properties. Among them,  $MoS_2$  has a layered structure similar to graphite and its large surface area, good electrical conductivity (metallic when in 1T phase), fast ionic conductivity and the 2D-like morphology that make it a potential candidate for high-performing electrode [23,24].

On the other hand, manganese dioxide ( $MnO_2$ ) is well-known to behave as ideal pseudocapacitor material, due to its fast-redox reactions, and can be used as efficient cathode [25–27].  $MnO_2$  can be easily electrodeposited onto current collectors by anodic or cathodic electrodeposition [28,29], and this soft-chemical method also makes it possible to conformally coat very rough current collectors. The most common morphology of  $MnO_2$  achievable by anodic electrodeposition is a porous nanostructured three-dimensional network [28,30,31] or a matrix of interconnected micro- and nano-scale fibers, rods and nanosheets [28,31,32]. Moreover, recently, the pseudocapacitive performance of manganese oxide with oxygen vacancies ( $MnO_{2-x}$ ) have been reported showing better values than bare  $MnO_2$  [33].

Herein, an asymmetric supercapacitor exploiting carbon fibers (CF) as current collectors,  $Mn_3O_4$  as the cathode,  $MoS_2$  as anode and polyvinyl alcohol (PVA) gel electrolyte is reported. The  $Mn_3O_4$  phase is achieved by combining electrodeposition of  $MnO_x$  on CF and its subsequent reduction by annealing the sample in an atmosphere rich in  $H_2$ .  $MoS_2$  instead was obtained by hydrothermal synthesis, and then dip coated onto the CF. In both cases, the CFs play an important role, allowing better exploitation of the active material, good material loading and flexibility. The asymmetric supercapacitor exhibits a wide potential window of 1.8 V, a high specific capacitance of  $70 \text{ F g}^{-1}$ , high energy and power density values, together with good cycling stability and bending stability.

## 2. Materials and Methods

### 2.1. Electrodeposition of Manganese Oxide and Annealing to Spinel $Mn_3O_4$

The deposition of  $MnO_x$  electrodes on carbon fibers was carried out by a simple 2-step galvanostatic electrodeposition in a three electrodes cell, where a Pt sheet and a Ag/AgCl sat. were used as counter and reference electrodes, respectively, as described elsewhere [34]. Before starting the electrodeposition, carbon fibers (Panex®35, ZOLTEK) were gently cleaned in an acetone, ethanol

and deionized water (1:1:1) ratio, and then blocked onto a microscope glass slide with a copper tape, to improve the electrical contact. The deposition was carried out under a current density of 1 mA/cm<sup>2</sup> for 45 min and 0.5 mA/cm<sup>2</sup> for 75 min in a solution containing 0.1 M manganese (II) acetate (Mn (CH<sub>3</sub>COO)<sub>2</sub>, > (98%), Sigma-Aldrich), as MnO<sub>2</sub> precursor, and 0.1 M of sodium sulfate (Na<sub>2</sub>SO<sub>4</sub>, 98%, Sigma-Aldrich), as supporting electrolyte. After the first step of 45 min, the electrodes were calcined for 1 h at 150 °C, while after the second step of 75 min deposition, the calcination was carried out at 300 °C for 1 h and a black layer of manganese oxide on fiber-electrodes was obtained with an average mass loading of 0.25 mg cm<sup>-1</sup>. The mass was estimated by weighting the carbon fibers before and after the electrodeposition. The thermal treatment of electrodeposited electrodes was carried out by annealing the fibers under a constant hydrogen flow at 250 °C for 3.5 h (2.5 °C per min ramp applied). After this treatment, the manganese oxide's stoichiometry changes to Mn<sub>3</sub>O<sub>4</sub>, as shown in the "Results and Discussion" section.

## 2.2. Synthesis of MoS<sub>2</sub> Flakes and Electrodes Fabrication

The synthesis of MoS<sub>2</sub> nanoflakes was carried out with a simple hydrothermal method, as described elsewhere [24]. A total of 20 mg of dried flakes of MoS<sub>2</sub> were sonicated in 10 mL distilled water, and the bundle of fibers was gently dipped into this dispersion and allowed to dry until the desired mass per length was obtained. No addition of binder was employed.

## 2.3. Physical-Chemical Characterization

The crystallographic characterization of the as-synthesized samples was performed with a Panalytical X'Pert MRD Pro in Bragg/Brentano configuration X-ray diffractometer (XRD) with a Cu K $\alpha$  X-ray source.

Raman spectrum was achieved using Renishaw InVia Reflex micro-Raman spectrometer (Renishaw plc, Wotton-under-Edge, UK), equipped with a cooled CCD camera, with a laser excitation wavelength of 514.5 nm and a laser spot size of 10  $\mu$ m.

The characterization of morphology was performed with a Field-Emission Scanning Electron Microscope (FESEM Supra 40, manufactured by Zeiss), equipped with an Oxford instruments Si (Li) detector for Energy Dispersive X-ray (EDX) spectroscopy.

X-ray photoelectron spectroscopy (XPS) measurements were performed with a Physical Electronics system (PHI 5000 Versa Probe), equipped with monochromatic X-ray Al K $\alpha$  (1486.6 eV energy) source and a combined e<sup>-</sup> and Ar<sup>+</sup> system for charge compensation. Different pass energy values were adopted for survey spectra (187.85 eV) and high-resolution scans (23.5 eV). The calibration of the binding energy scale was obtained by assigning an energy value of 284.8 eV to the main contribution (C-C) of the C 1s region. Background subtraction in high-resolution scans was performed by means of a Shirley function. Data analysis was carried out with Casa XPS software. Transmission electron microscopy (TEM) analyses were performed on an FEI Tecnai F20 ST transmission electron microscope.

## 2.4. Electrochemical Characterization and Device Assembling

The storage behavior of the individual electrodes, Mn<sub>3</sub>O<sub>4</sub> and MoS<sub>2</sub> coated fibers, was studied in a three electrodes cell in 1 M Na<sub>2</sub>SO<sub>4</sub> electrolyte, purged with nitrogen for 20 min prior to any measurement. Platinum bar and Ag/AgCl sat. KCl were employed as counter and reference electrodes respectively. Cyclic voltammetry at multiple scan rates was carried out between -0.6 V and 0.15 V vs. Ag/AgCl and between 0.1 V and 0.85 V vs. Ag/AgCl for MoS<sub>2</sub> and Mn<sub>3</sub>O<sub>4</sub> electrodes, respectively. AC impedance spectroscopy was carried out at 5 mV amplitude between 100 kHz and 10 mHz. In the asymmetric devices the mass or length of the MoS<sub>2</sub> decorated carbon fibers electrode was tuned, in order to counterbalance the charges stored on the Mn<sub>3</sub>O<sub>4</sub> electrode and the potential voltage window was determined. An asymmetric device was first characterized in 1M Na<sub>2</sub>SO<sub>4</sub> electrolyte by means of cyclic voltammetry and chronopotentiometry in 1.8 V voltage window. An asymmetric device was also fabricated in two parallel electrodes configuration using hydrogel

electrolyte (the gelification of the liquid electrolyte was done by adding PVA (89,000–98,000, 99+% hydrolyzed Sigma Aldrich) in 1M Na<sub>2</sub>SO<sub>4</sub> Sigma Aldrich). The anode (MoS<sub>2</sub>) and cathode (Mn<sub>3</sub>O<sub>4</sub>) were first dipped in hydrogel and left in ambient condition for 30 min for semi-solidification. Then, both the electrodes were put between two kapton<sup>®</sup> tapes in parallel configuration and sealed. Characterization was also performed for this device by means of cyclic voltammetry, chronopotentiometry in 1.8 V voltage window. Moreover, to appreciate the potentialities of those devices, the capacitance retention was studied at different bending angles. All the experiments were performed with a Metrohm Autolab PGSTAT128 Potentiostat/Galvanostat and Nova 2.1 software.

### 3. Results and Discussion

#### 3.1. Characterization of the Material at the Cathode

Binder-free highly porous Mn<sub>3</sub>O<sub>4</sub> nanoflakes were obtained via a 2-step process, which involved the galvanostatic electrodeposition of the manganese oxide and its surface modification through hydrogenation.

The description of the first fabrication step is reported in [35]; herein, a further improvement is presented, where the MnO<sub>x</sub> decorated carbon fibers were exposed to a thermal treatment at 250 °C under hydrogen flow for 3.5 h. As shown in Figure 1a, the electrodeposition process does not produce any cracks in the manganese oxide film, and a uniform coverage of nanosheets (Figure 1c) is obtained, in accordance with the previous literature [36,37]. EDX analysis of the electrodeposited manganese oxide electrode (Figure 1b) confirms the expected chemical composition showing C, O and Mn X-ray peaks, with a negligible contribution by Si, which can be ascribed to the internal fluorescence of the Si(Li) detector or surface contamination. It is interesting to notice that, after the thermal treatment, a modification of the surface of the nanosheets is obtained (Figure 1d), resulting in increased roughness and, consequently, an increased surface area of the electrode. This trend is further confirmed by the electrical double layer capacitance value which is proportional to the active surface area (see Figure S1, supporting information). In order to identify a possible phase transformation during this treatment, X-ray diffraction analysis was performed. The thermal treatment under hydrogen flow induces a crystallization of the material to Mn<sub>3</sub>O<sub>4</sub> in the spinel form (weak signal), as clearly evidenced in the XRD pattern reported in Figure 2a. As reported previously [35], the manganese oxide film is amorphous after the electrodeposition process, while after the hydrogenation, it is possible to identify peaks from the (101), (112), (103) and (201) planes of the Mn<sub>3</sub>O<sub>4</sub> crystallographic structure, superimposed to the typical diffraction pattern of CFs.

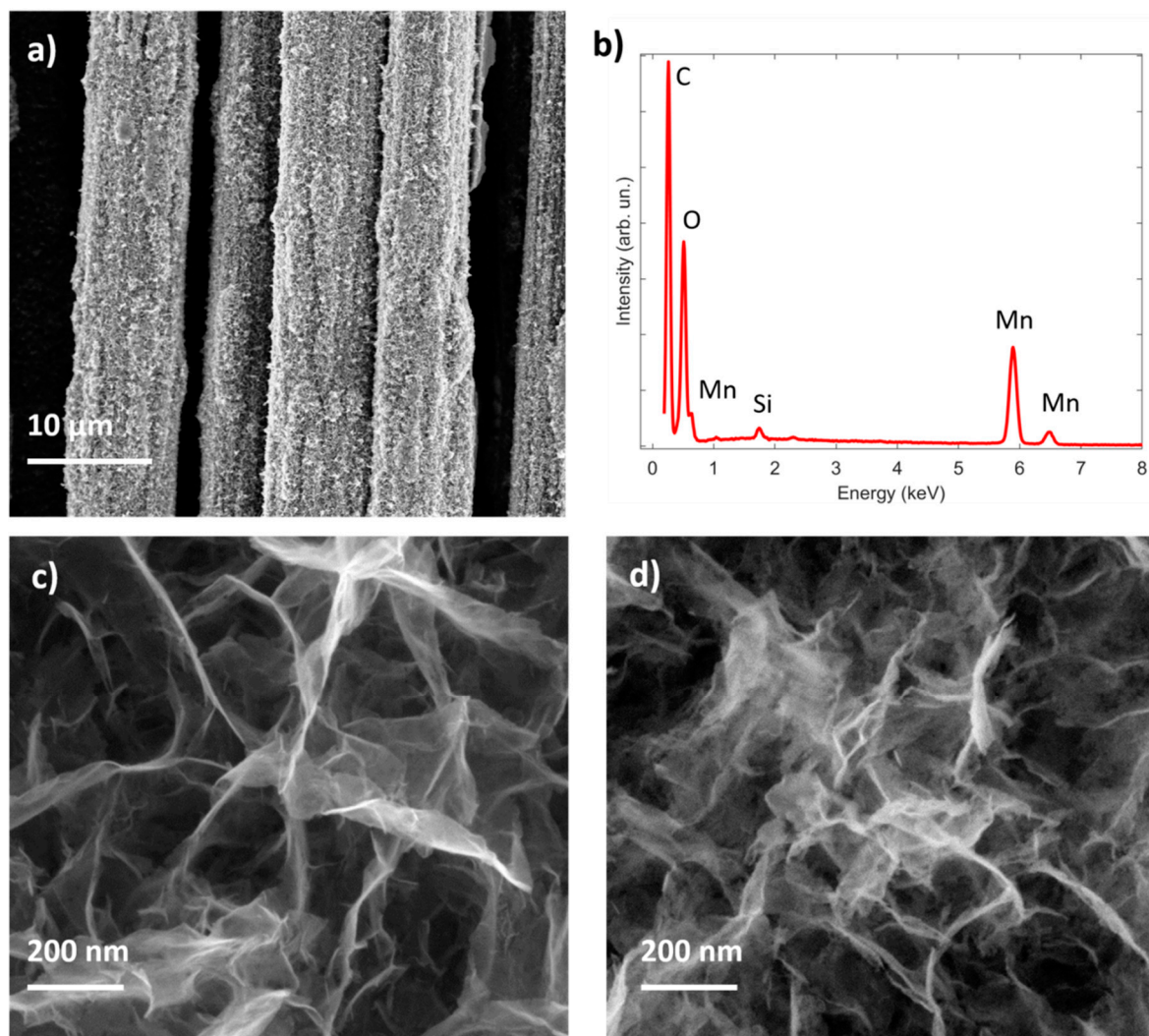


**Figure 1.** (a) Field-Emission Scanning Electron Microscope (FESEM) image of the 2-step electrodeposited manganese oxide showing good coverage of the carbon fibers and (b) representative Energy Dispersive X-ray (EDX) spectrum; higher magnification FESEM images of the 2-step electrodeposited manganese oxide before (c) and after (d) the thermal treatment in H<sub>2</sub>.

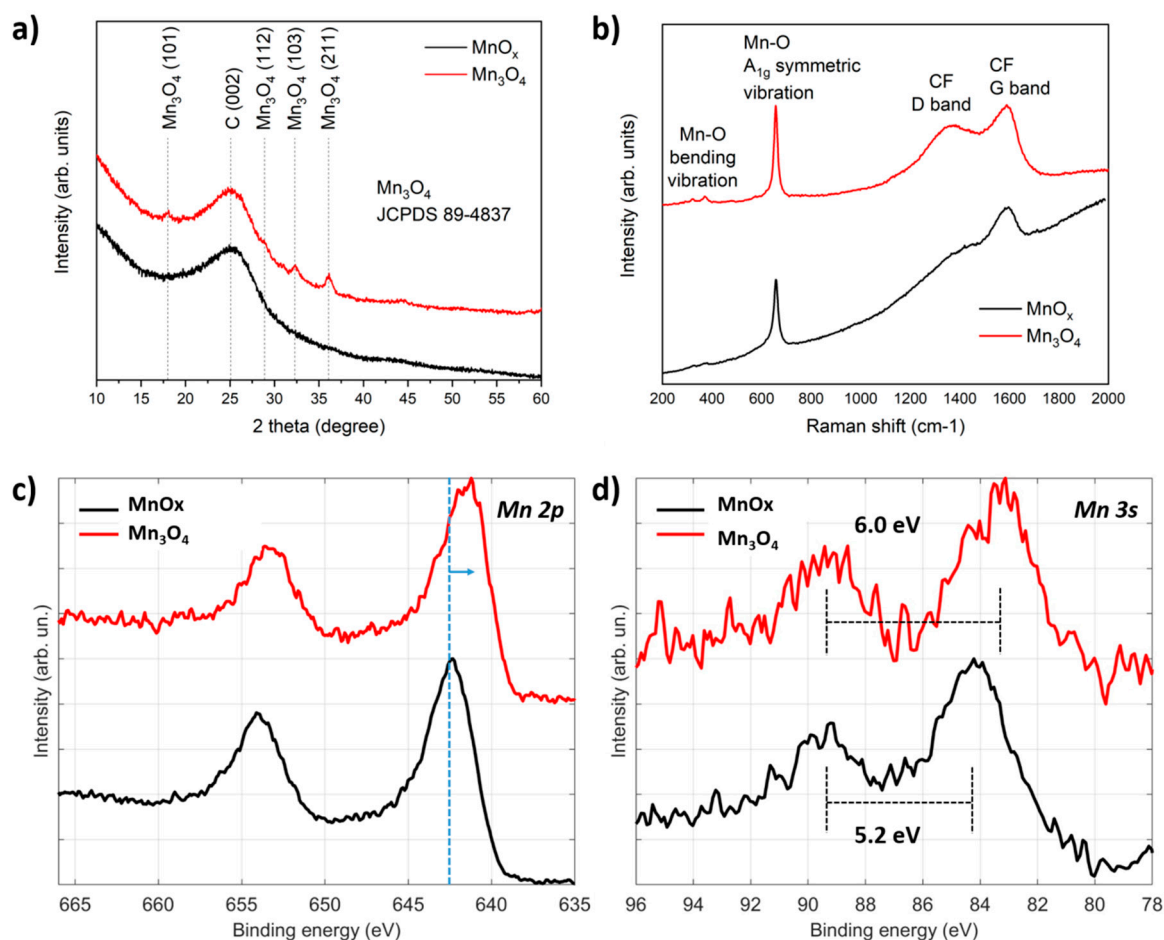


**Figure 2.** (a,b) Show the XRD and Raman spectra of  $\text{MnO}_x$  and  $\text{Mn}_3\text{O}_4$ , (c,d) provide XPS spectra of Mn 2p and Mn 3s regions of manganese oxide before ( $\text{MnO}_x$ ) and after ( $\text{Mn}_3\text{O}_4$ ) the thermal treatment in  $\text{H}_2$ .

Raman spectroscopy is less sensitive in the precise identification of the crystallographic behavior of this material, since it is well-established [35,36] that  $\text{MnO}_x$  in their different crystalline forms exhibit Raman signals associated to the motion of the oxygen atoms within the  $\text{MnO}_6$  octahedral units in  $\text{MnO}_x$ . The spectrum reported in Figure 2b exhibits an intense and sharp peak at  $657\text{ cm}^{-1}$ , which can be ascribed to  $A_{1g}$  mode which corresponds to the Mn–O breathing vibration of  $\text{Mn}^{2+}$  ions in tetrahedral coordination, and two weak features at  $371$  and  $318\text{ cm}^{-1}$ , respectively, related to Mn–O bending vibrations. Such features are more evident after calcination, but are visible also in the pristine material. Thermal process in  $\text{H}_2$  strongly reduces the luminescence emission, related with the growing behavior for high wavenumbers superimposed to the spectrum in pristine material.

A major contribution to unravel the composition of the annealed manganese oxide was given by XPS to study the change in surface composition. In fact, the Mn 2p and Mn 3s regions of the photoelectron spectrum provide useful information for the phase identification of manganese oxide species. Regarding the Mn 2p region (Figure 2c), a shift to lower binding energy of the Mn  $2p_{3/2}$  peak after the hydrogen treatment suggests a decrease in the oxidation state of Mn, in accordance with the literature [37–39]. Moreover, the absence of shake-up satellites at the higher binding energy side of the Mn  $2p_{3/2}$  peak excludes the presence of the MnO in significant amounts [40]. In the Mn 3s spectrum (Figure 2d) of the untreated manganese oxide and of the sample after annealing in  $\text{H}_2$  flow, a substantial change in the energy difference of the multiplet split components is shown, due to a change in the oxidation state. The larger the energy difference  $\Delta E$  of the multiplet split components, the lower the Mn average oxidation state (AOS), according to the formula  $\text{AOS} = 8.95 - 1.13 \cdot \Delta E$  [41]. The  $\text{Mn}_3\text{O}_4$  sample shows a larger  $\Delta E$  (6 eV) as compared to (5.2 eV) for the untreated manganese

oxide sample, indicating a decrease in AOS from 3.1 ( $\text{MnO}_x$ ) to 2.2 ( $\text{Mn}_3\text{O}_4$ ), based on the previously reported formula. In summary, XPS confirms that the  $\text{H}_2$  treatment lowers the average oxidation state of Mn atoms, in accordance with the structural characterization and with the literature [33].

### 3.2. Characterization of the Material at the Anode

Figure 3a shows a schematic representation of the fabrication of the anode electrode, in which  $\text{MoS}_2$  nanoflakes were dip-coated on carbon fiber. The  $\text{MoS}_2$  nanoflakes were hydrothermally synthesized using phosphomolybdic acid and L-Cysteine as precursors in an autoclave at 180 °C for 12 h (details are provided in the experimental section), according to the procedure previously published [24]. Through this particular synthetic approach, it is possible to obtain few-layer nanoflakes with thickness  $<5$  nm and lateral size  $<100$  nm (Figure 3b). Electrodes which exhibit 2D morphology and, in particular, transition metal dichalcogenides (TMD) are well known to be highly efficient for a rapid electron/ion transport [42]. The open structure allows fast variations of the volume, thus increasing the stability of the electrodes upon charge and discharge cycles, even when subjected to intercalation of ions [43]. Based on the electron diffraction measurements (Figure 3c), the nanoflakes exhibit a layered structure ( $\sim 6.1$  Å interplanar spacing (002)), and the absence of in-plane ordering (diffused rings in the diffraction pattern). Further information on the structure is obtained from XPS, where two sets of peaks separated by 0.9 eV in binding energy [23], [44] in the  $\text{Mo3d}/\text{S2s}$  (Figure 3d) and  $\text{S2p}$  (Figure 3e) regions of the photoelectron spectrum point to the presence of short range domains of 1T and 2H polymorphs with a ratio 1T/2H $\sim$ 2.2. This is particularly interesting for applications of mixed-phase 1T-2H  $\text{MoS}_2$  nanostructures, because the presence of the metallic (1T) phase assures a better electron conductivity than only semi-conductive structures (2H), and this leads to much faster charge transfer kinetics at the nanosheets [45].



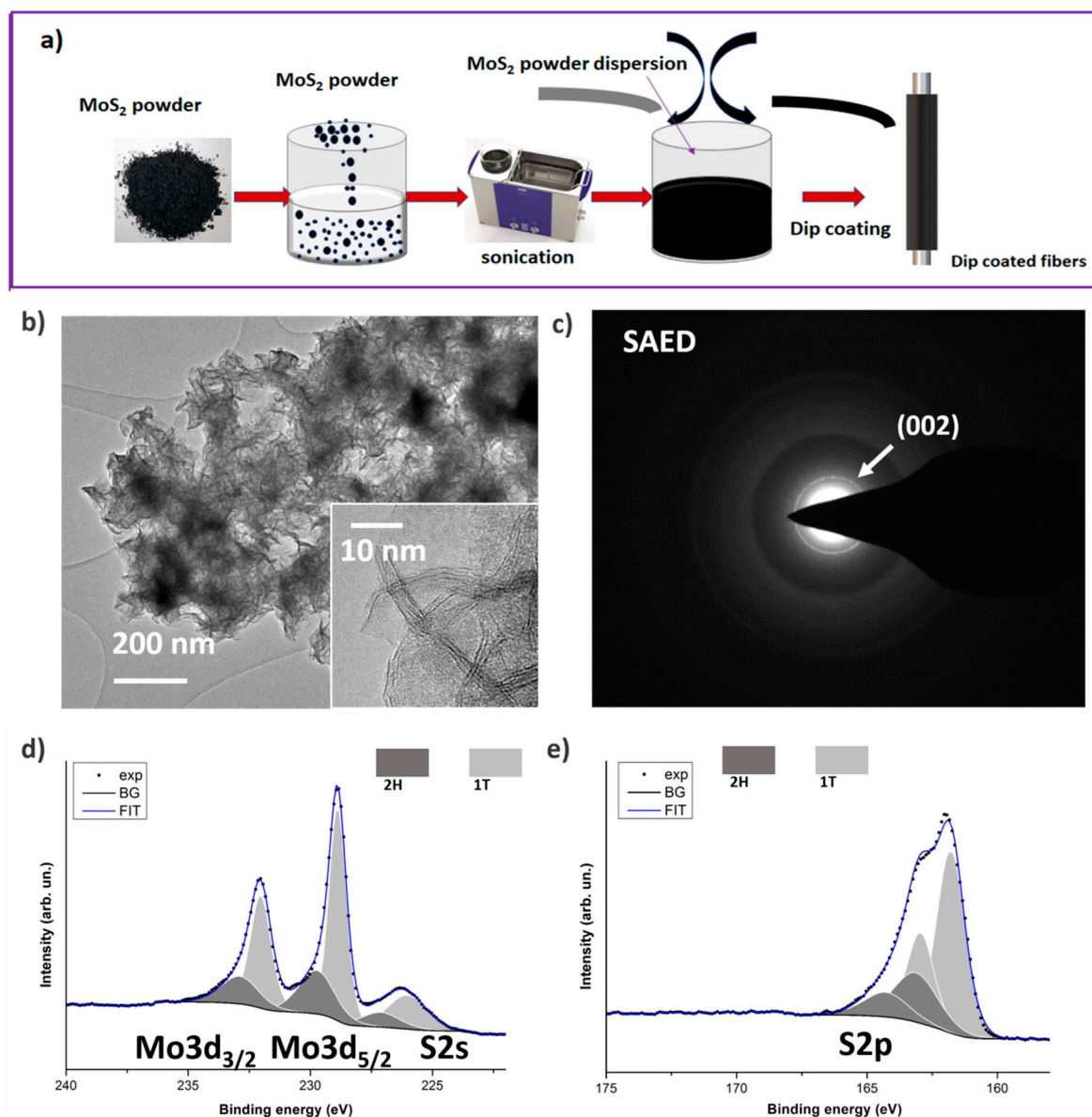


**Figure 3.** (a) Schematic representation of dip-coating of MoS<sub>2</sub> on carbon fiber (CF); (b) shows a low-magnification TEM image of the MoS<sub>2</sub> nanoflakes, while the inset provides a high-magnification image showing the layered structure of the nanoflakes, (c) provides a representative electron diffraction pattern. XPS high-resolution scans of Mo3d/S2s region (d) and S2p region (e) for MoS<sub>2</sub> nanoflakes are presented.

### 3.3. Electrochemical Characterization

The behavior of MoS<sub>2</sub> and Mn<sub>3</sub>O<sub>4</sub> electrodes for supercapacitors was first investigated in 1M Na<sub>2</sub>SO<sub>4</sub> in a three electrodes configuration, in which the modified fibers were used as the working electrodes and a platinum bar and a saturated Ag/AgCl were employed as counter and reference. In Figure 4a, the cyclic voltammetries at 5 mV s<sup>-1</sup> of the two samples are shown together, in order to appreciate their compatible voltage windows. In this experiment, the length of the MoS<sub>2</sub> electrode was increased with respect to the Mn<sub>3</sub>O<sub>4</sub>, in order to equilibrate the charges stored by the two electrodes. The performance of the Mn<sub>3</sub>O<sub>4</sub> electrode was studied and compared with the behavior of the same sample prior to thermal treatment, and the Mn<sub>3</sub>O<sub>4</sub> electrode has shown better performance than the latter (see Figure S1, supporting information). Mn<sub>3</sub>O<sub>4</sub> electrodes were tested between 0.1 V and 0.85 V vs. Ag/AgCl showing quasi-rectangular shapes at all the scan rates employed. The capacitive performances of the MoS<sub>2</sub> electrode relies in the mixed 1T-2H phases obtained by simple

hydrothermal synthesis of the flakes that are nicely attached onto the carbon fibers without any binder [23]. Cyclic voltammograms acquired at different scan rates show a potential window from -0.6 V to +0.15 V vs. Ag/AgCl. In Figure 4b, the specific capacitance values of the two electrodes are shown. According to this plot, for MoS<sub>2</sub> electrodes, the capacitance remains almost constant up to 20 mV s<sup>-1</sup>, and for slower scan rates it increases. For the Mn<sub>3</sub>O<sub>4</sub> samples, the capacitance rises with the decrease of the scan rate, therefore, the total amount of stored charges is strongly time dependent. In order to understand the storage mechanisms of the two different electrodes, the total charge has to be separated in three components: (i) the non-faradaic currents due to the double-layer; (ii) near-surface adsorption giving rise to the pseudocapacitance; and (iii) the faradaic currents rising from charge transfer and diffusion of ions inside the structure; [25,46,47]. As the first two phenomena are capacitive-controlled, with the current proportional to the scan rate ( $v$ ) while the latter is diffusion-controlled, the current is proportional to the square root of the scan rate ( $v^{1/2}$ ). At each potential, the current  $i(V)$  can be divided in two contributions that are capacitive controlled ( $k_a v$ ) and diffusion-controlled ( $k_b v^{1/2}$ ):

$$i(V) = k_a \cdot v + k_b \cdot v^{1/2} \quad (1)$$

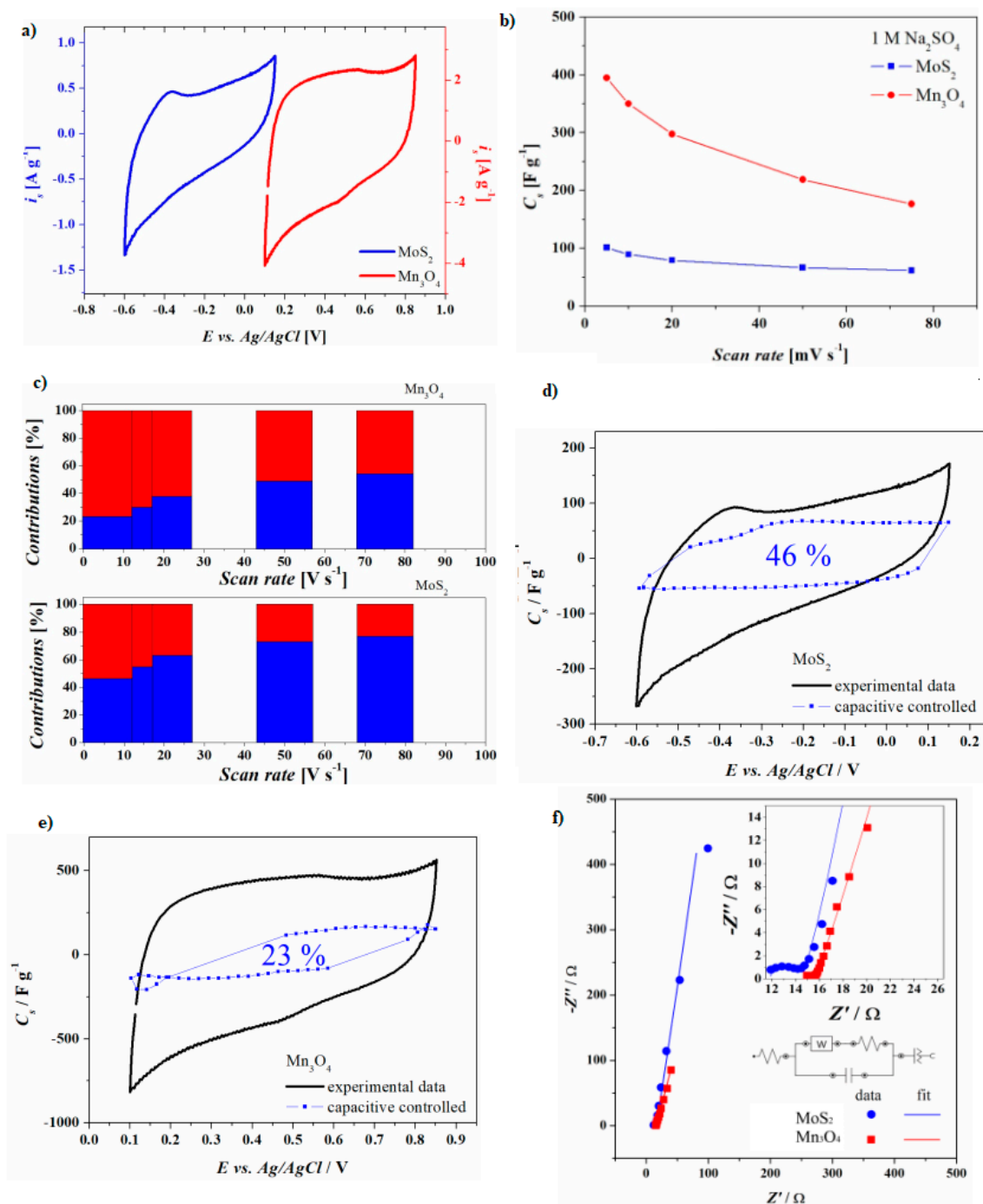
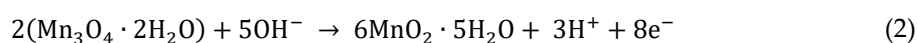


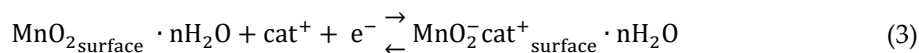
**Figure 4.** Comparison of cyclic voltammetry (a), comparison of specific capacitances of MoS<sub>2</sub> (blue graphs, 0.85 mg) and Mn<sub>3</sub>O<sub>4</sub> (red graphs, 0.4 mg) electrodes (b). Estimation of the charge stored by diffusion-controlled phenomena (red) and capacitive controlled phenomena (blue) at different scan rates on MoS<sub>2</sub> (lower graph) and Mn<sub>3</sub>O<sub>4</sub> (upper graph) electrodes (c), comparison of experimental data with computed data for MoS<sub>2</sub> and Mn<sub>3</sub>O<sub>4</sub> electrodes, respectively (d,e), AC impedance spectroscopy and Nyquist plot up to 10 mHz of the MoS<sub>2</sub> electrode (blue) and Mn<sub>3</sub>O<sub>4</sub> electrodes red (f), inset shows the equivalent circuit of electrode, respectively.

This method makes it possible to divide the fraction of current due to capacitive effects (EDLC and pseudocapacitance) and the fraction due to intercalation/insertion of cations in the active material. In the MoS<sub>2</sub> electrodes, the capacitive controlled mechanism is predominant for scan rates higher than 10 mV s<sup>-1</sup> (55 %), while in the Mn<sub>3</sub>O<sub>4</sub> electrodes, it is predominant for scan rates higher than 50 mV s<sup>-1</sup> (58%). For lower scan rates, the diffusion-controlled current becomes predominant, as clearly seen in the red plots in Figure 4c, where the partition of the charges due to the two

phenomena are visualized as a percentage of the total charge. Figure 4d,e shows the experimental voltammetry (black line) with the simulated capacitive-controlled current (blue line and dots), for the MoS<sub>2</sub> and Mn<sub>3</sub>O<sub>4</sub> electrodes, respectively. In the simulated curve, the presence of dots indicates a  $\chi^2$  larger than 0.9 in the fitting procedure. The charge-storage mechanism in Mn<sub>3</sub>O<sub>4</sub> is similar to that of untreated MnO<sub>x</sub>, with Faradic reactions occurring both on the surface and in the bulk of the electrode. The surface Faradaic reaction involves the adsorption/desorption of alkali metal cations (called cat<sup>+</sup> such as H<sup>+</sup>, Li<sup>+</sup>, Na<sup>+</sup>, K<sup>+</sup>) on the manganese oxide in neutral electrolyte. In both mechanisms of charge-storage, redox reactions between the 2+, 3+, and 4+ oxidation states of Mn ions occur [48]. Differently from the well-known ideal rectangular shape of double-layer capacitors, in Mn<sub>3</sub>O<sub>4</sub> a pair of peaks are easily distinguished at 0.48 V and 0.56 V, which are rising from the redox transitions of Mn between multiple valence states counterbalanced by the intercalation/deintercalation of cations [49,50] in the spinel 3D-tunnels of the material. The spinel's open structure, in fact, improves the diffusion inside the Mn<sub>3</sub>O<sub>4</sub> microstructure [51,52]. In neutral electrolytes, the suggested reaction path and storage mechanisms are [53]:



The efficiency conversion of this reaction step is highly dependent on the preconditioning time (or number of cycles when cyclic voltammetry is employed). Herein, the Mn<sub>3</sub>O<sub>4</sub> electrodes reached a stable voltammetry after 300 cycles. The reversible reactions are:

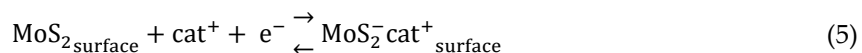


In the previous literature, this mechanism was suggested to be predominant in amorphous MnO<sub>2</sub>, or when the sample presents large specific surface area [47,54], and it was associated with optimal particle size and pore distribution. The second mechanism was suggested [47,55,56] to be predominant for crystalline MnO<sub>2</sub>, in which the crystallographic cell provide tunnels in which limited Faradaic reactions with intercalation/deintercalation of cations in the electrolyte takes place:

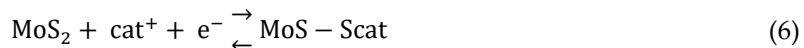


In this particular compound, both charge storage mechanisms (2) and (3) take place: the first due to the open channels of the spinel structure, which offer a large surface area, and the second for deeper thicknesses. According to the time-dependent data analysis previously described, the diffusion-controlled capacitance is significantly high in the sample Mn<sub>3</sub>O<sub>4</sub> and it dominates also at fast rates (50 mV s<sup>-1</sup>). The main mechanism is therefore the intercalation/deintercalation of cations or protons into/out the Mn<sub>3</sub>O<sub>4</sub> nanostructures. The quasi-rectangular shape of the voltammeteries at all the scan rates indicates a fast charge/discharge process that happens at an almost constant rate, even for solid state diffusions. This may be due to the thermal treatment in hydrogen atmosphere that enhances the surface porosity and generates high surface area with more active Mn (II) and Mn (III) sites for a rapid intercalation and extraction of cations.

In MoS<sub>2</sub>, the quasi-rectangular nature of the CV curves indicates the capacitive behavior of such electrodes. The deviation from a perfect rectangular behavior can be attributed to the electrosorption of protons on the surface of the nanosheets [56]. The adsorption of H<sup>+</sup> leads, in fact, to the formation of molecular hydrogen and evolution of the gas, not only in acidic media [45,57,58], but also in neutral electrolytes [59]. As discussed above in the XPS and TEM paragraphs, the hydrothermal synthesis employed in this study makes it possible to obtain a mixed 1T-2H phase of MoS<sub>2</sub>, and the electrodes were obtained simply by dip coating the suspension on the carbon fibers with no binder addition. This makes it very challenging to identify a univocal onset potential of the HER from sample to sample and therefore to decide the lower potential limit of the voltammetry. In 2D-MoS<sub>2</sub> flakes, the nature of the storage mechanisms [59,60] are the formation of the electrical double layer with the adsorption/desorption of ions:



and the pseudocapacitance [23,61] with the insertion/extraction of protons and alkali cations between the interlayer spaces:



Both these two phenomena are capacitive-controlled in nature, which is in fact the main contribution to the total current of MoS<sub>2</sub> samples (Figure 4c), unless very slow rates of charge and discharge are applied. When very slow voltammetry is performed, different phenomena start to take place and get over. This current can be due to diffusion phenomena that mainly take place on the MoS<sub>2</sub> and, to some extent, on the carbon fiber substrate that is partially exposed to the solution due to the absence of a binder or a compact/blocking layer, as it has been observed for different carbonaceous materials [61]. AC impedance measurement was carried out at the open circuit potentials of each electrode as shown in Figure 4f. From the data fitting, it is possible to appreciate the uncompensated resistance (highest frequencies) characteristic of each material-interfaces, the constant phase element (lower frequencies) that mimic imperfect capacitor (EDLC and pseudocapacitance) and the Randles' circuit in which the Warburg impedance (medium frequencies) describes the diffusion-controlled phenomena previously analyzed and commented in the text. The uncompensated resistance is 14.6 Ω and 11.9 Ω for the Mn<sub>3</sub>O<sub>4</sub> and MoS<sub>2</sub> electrodes, respectively, while the charge transfer resistance values of 0.9 Ω and 2.5 Ω suggest fast electron transfer in both materials.

After the study of the single electrodes, the MoS<sub>2</sub> electrode was employed as an anode and the Mn<sub>3</sub>O<sub>4</sub> was placed as a cathode in asymmetric supercapacitors. With this intent, two configurations of asymmetric supercapacitors were chosen: (i) a standard asymmetric device by using 1M Na<sub>2</sub>SO<sub>4</sub> electrolyte (called liquid electrolyte) and (ii) an asymmetric device by using PVA based gel (called hydrogel) in order to make the cell appealing for commercial flexible device with large bending stability over multiple angles. Figure 5a shows the comparison of charge-discharge profiles (upper graph) and CV (lower graph) of the devices in liquid electrolyte and in hydrogel electrolyte. The two methods show consistent behaviors at multiple current densities and scan rates: as shown in Figure 5b, the specific capacitance estimated from the galvanostatic experiments and from cyclic voltammetries show that the devices made with hydrogel have larger capacitance at low rates, while the liquid electrolyte devices provide larger capacitance even at faster rates. Decreasing the rates of the experiments, the capacitance values of the two devices merge to quite the same value (i.e., the specific capacitances at 0.5 A g<sup>-1</sup> are 65 F g<sup>-1</sup> and 70 F g<sup>-1</sup>). Wearable and flexible devices are those in which the performances of the devices remain almost invariant when the electrodes are bended, folded and wrapped. The presence of liquid electrolyte soaked in a membrane is a major limitation on the flexibility, because by bending the device (i) the electrolyte moves and this creates inhomogeneity at the electrode-electrolyte interface and (ii) the roughness of the membrane scratches the active material away from the fibers. With this aim, the devices with hydrogel were aged (shown in Figure 5c bottom). From the bending experiments, it was observed that the capacitance decreased of 12% with respect to the initial value, when the device was completely folded (180°). The devices with hydrogel were cycled at 200 mV s<sup>-1</sup> up to 3000 scans, showing a capacitance retention of 80%, which could be increased indeed by improving the packaging and sealing. The performances of the two devices are compared in Figure 5d, with the literature on supercapacitors in which MoS<sub>2</sub> and MnO<sub>2</sub> were employed on steady Ni-foam current collectors and cellulose separator soaked of hydrogel [62], bendable supercapacitors in which one of the electrodes includes a flexible carbon-based current collector decorated with MoS<sub>2</sub> [63–69] with Mn<sub>3</sub>O<sub>4</sub> [70–75], or specifically with carbon fibers coated with MnO<sub>2</sub> [76,77]. In particular, at powers from 9000 to 450 W/kg, the device in this study based on liquid electrolyte delivers from 14 to 29 Wh/kg, while that with hydrogel delivers 1 to 31 Wh/kg.

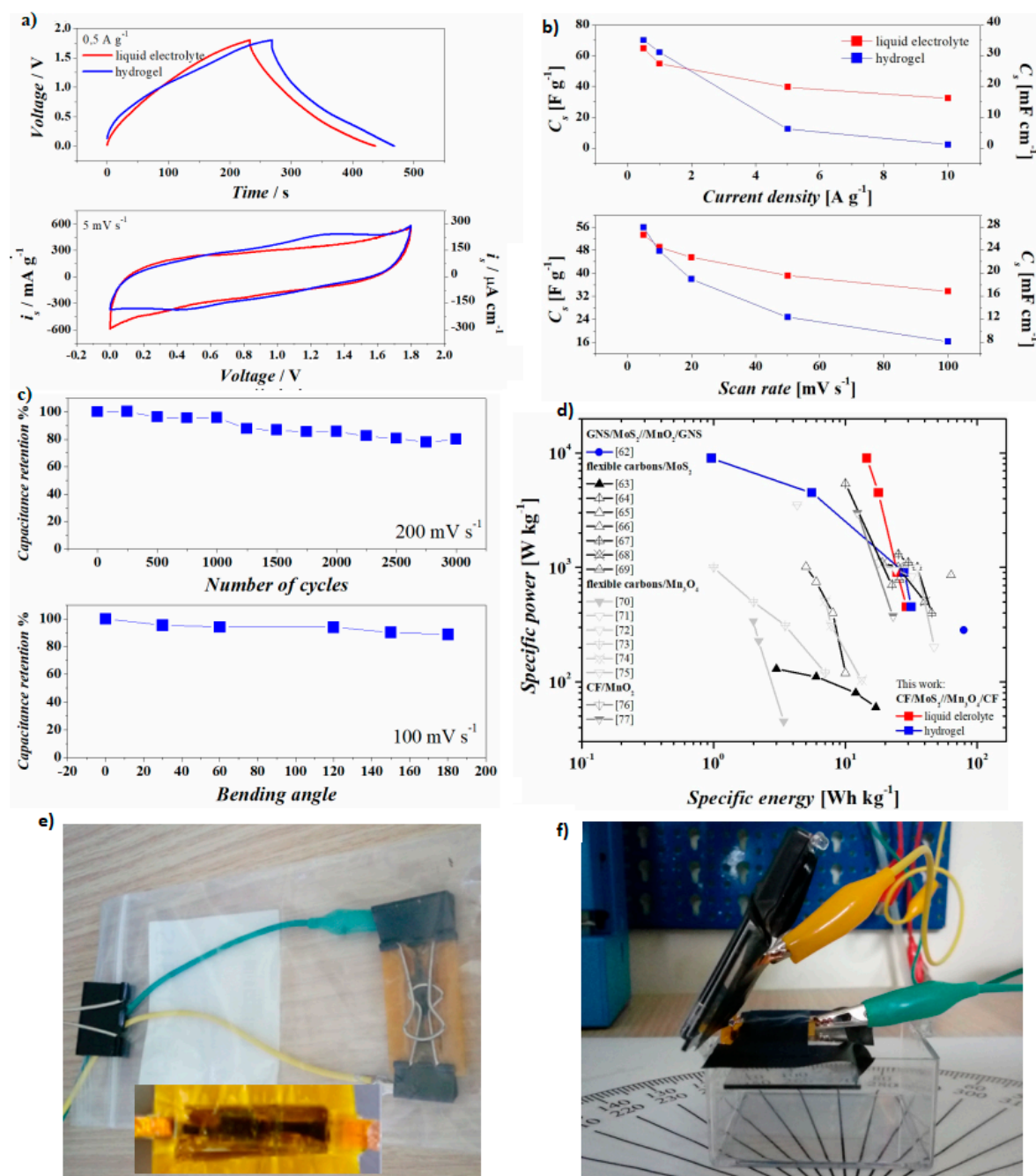


**Figure 5.** Electrochemical experiments on flexible devices employing liquid electrolytes (blue) and hydrogel (red): (a) charge and discharge at  $0.5 \text{ A g}^{-1}$  (upper) and cyclic voltammetry at  $5 \text{ mV s}^{-1}$  (lower), (b) specific capacitance estimated on charge and discharge experiments (upper) and on cyclic voltammetry (lower), (c) cyclability and bending stability, (d) Ragone plot and the pictures of the device with hydrogel during ageing (inset shows the device) (e) and bending (f) tests.

#### 4. Conclusions

$\text{Mn}_3\text{O}_4$  on carbon fibers has been fabricated by anodic electrodeposition and annealing in reducing atmosphere and used as flexible cathode. Two-dimensional flakes of mixed phase 1T-2H  $\text{MoS}_2$  were synthesized by hydrothermal method and they were employed as binder-free active material on carbon fibers as flexible anode. Asymmetric supercapacitors assembled with neutral electrolyte deliver at  $0.5 \text{ A g}^{-1}$  a device capacitance of  $65 \text{ F g}^{-1}$  ( $32 \text{ mF cm}^{-1}$ ), and when the gel electrolyte is employed, it increases up to  $70 \text{ F g}^{-1}$  ( $35 \text{ mF cm}^{-1}$ ). The latter layout makes it possible not only to achieve higher level of capacitance, but also to use such device under bending conditions with limited capacitance fading also after 3000 cycles. The present results demonstrate that these

flexible hybrid devices which involve all the electrochemical storage mechanisms can increase the typical energy range and maintain the same speed (power) of supercapacitors.

**Supplementary Materials:** The following are available online at [www.mdpi.com/2079-4991/10/6/1084/s1](http://www.mdpi.com/2079-4991/10/6/1084/s1), Figure S1: (a,b) cyclic voltammetries recorded at different scan rates for both  $\text{MnO}_x$  and  $\text{Mn}_3\text{O}_4$  (before and after thermal treatment, respectively), (c,d) cyclic voltammetries and capacitance comparison for  $\text{MnO}_x$  and  $\text{Mn}_3\text{O}_4$ , Table S1: comparison of voltage windows and specific capacitances

**Author Contributions:** Conceptualization of the supercapacitor design, electrodes assembly, and electrochemical characterization, interpretation of results, writing and editing M.S.; TEM, FESEM and XPS analyses, interpretation, writing and editing M.F.; XRD and Raman measurements with interpretation and editing S.B.; participation in most of the experimental data interpretation, supervision and participation in manuscript writing and editing C.F.P. and A.L.; synthesis of  $\text{Mn}_3\text{O}_4$  U.Z.; synthesis of  $\text{MoS}_2$  P.R.; participation in the synthesis, electrode fabrication, device fabrication, electrochemical characterization and writing main draft A.R. All authors have read and agreed to the published version of the manuscript.

**Funding:** This research received no external funding and all the research activities are funded by Politecnico Di Torino Italy.

**Conflicts of Interest:** The authors declare no conflict of interest.

## Reference

1. Wu, Z.; Li, L.; Yan, J.; Zhang, X. Materials Design and System Construction for Conventional and New-Concept Supercapacitors. *Adv. Sci. News* **2017**, *4*, 1600382.
2. Jayalakshmi, M.; Balasubramanian, K. Simple capacitors to supercapacitors-an overview. *Int. J. Electrochem. Sci.* **2008**, *3*, 1196–1217.
3. Miller, J.R.; Simon, P. Electrochemical capacitors for energy management. *Science* **2008**, *321*, 651–652.
4. Liu, J.; Li, Y.; Huang, X.; Ding, R.; Hu, Y.; Jiang, J.; Liao, L. Direct growth of  $\text{SnO}_2$  nanorod array electrodes for lithium-ion batteries. *J. Mater. Chem.* **2009**, *19*, 1859–1864.
5. Lukatskaya, M.R.; Dunn, B.; Gogotsi, Y. Multidimensional materials and device architectures for future hybrid energy storage. *Nat. Commun.* **2016**, *7*, 12647.
6. Brezesinski, T.; Wang, J.; Tolbert, S.H.; Dunn, B. Ordered mesoporous  $\alpha\text{-MoO}_3$  with iso-oriented nanocrystalline walls for thin-film pseudocapacitors. *Nat. Commun.* **2010**, *9*, 146–151.
7. Zhanga, L.L.; Zhao, X.S. Carbon-based materials as supercapacitor electrodes. *Chem. Soc. Rev.* **2009**, *38*, 2520–2531.
8. Xie, K.; Wei, B. Nanomaterials for stretchable energy storage and conversion devices. *Nanomater. Sustain. Energy* **2016**, 159–191, doi:10.1007/978-3-319-32023-6\_4.
9. Dai, Z.; Peng, C.; Chae, J.H.; Ng, K.C.; Chen, G.Z. Cell voltage versus electrode potential range in aqueous supercapacitors. *Sci. Rep.* **2015**, *5*, 9854, 2015.
10. Choudhary, N.; Li, C.; Moore, J.; Nagaiah, N.; Zhai, L.; Jung, Y.; Thomas, J. Asymmetric Supercapacitor Electrodes and Devices. *Adv. Mater.* **2017**, *29*, 1605336.
11. Choudhary, N.; Li, C.; Chung, H.-S.; Moore, J.; Thomas, J.; Jung, Y. High-Performance One-Body Core/Shell Nanowire Supercapacitor Enabled by Conformal Growth of Capacitive 2D  $\text{WS}_2$  Layers. *ACS Nano* **2016**, *10*, 10726–10735.
12. Graeme, C.; Lotya, M.; Cucinotta, C.S.; Sanvito, S.; Bergin, S.D.; Menze, R.; Shaffer, M.S.P.; Coleman, J. N. Solvent exfoliation of transition metal dichalcogenides: Dispersibility of exfoliated nanosheets varies only weakly between compounds. *ACS Nano* **2012**, *6*, 3468–3480.
13. Lou, W.; Chen, M.; Wang, X.; Liu, W. Novel single-source precursors approach to prepare highly uniform  $\text{Bi}_2\text{S}_3$  and  $\text{Sb}_2\text{S}_3$  nanorods via a solvothermal treatment. *Chem. Mater.* **2007**, *19*, 872–878.
14. Fang, L.; Qiu, Y.; Zhai, T.; Wang, F.; Lan, M.; Haung, K.; Jing, Q. Flower-like nanoarchitecture assembled from  $\text{Bi}_2\text{S}_3$  nanorod/ $\text{MoS}_2$  nanosheet heterostructures for high-performance supercapacitor electrodes. *Colloids Surf. A Physicochem. Eng. Asp.* **2017**, *535*, 41–48.
15. Tsai, H.-W.; Yagoubi, A.; Chan, T.-C.; Wang, C.-C.; Liu, W.-T.; Liao, C.-N.; Lu, S.-Y.; Chen, L.-J.; Chueh, Y.-L. Electrochemical synthesis of ultrafast and gram-scale surfactant-free tellurium nanowires by gas-solid transformation and their applications as supercapacitor electrodes for p-doping of graphene transistors. *Nanoscale* **2015**, *7*, 7535–7539.



16. Karade, S.S.; Sankapal, B.R. Two dimensional cryptomelane like growth of MoSe<sub>2</sub> over MWCNTs: Symmetric all-solid-state supercapacitor. *J. Electroanal. Chem.* **2017**, *802*, 131–138.
17. Peng, H.; Wei, C.; Wang, K.; Meng, T.; Ma, G.; Lei, Z.; Gong, X. Ni<sub>0.85</sub>Se@MoSe<sub>2</sub> Nanosheet Arrays as the Electrode for High-Performance Supercapacitors. *ACS Appl. Mater. Interfaces* **2017**, *9*, 17067–17075.
18. Iu, M.L.; Wang, X.; Huang, Z.; Guo, P.; Wang, Z. In-situ solution synthesis of graphene supported lamellar 1T'-MoTe<sub>2</sub> for enhanced pseudocapacitors. *Mater. Lett.* **2017**, *206*, 229–232.
19. Liu, M.; Wang, Z.; Liu, G.; Jiao, D.; Li, Y.; An, C.; Jun, Z. Synthesis of few-layer 1T'-MoTe<sub>2</sub> ultrathin nanosheets for high-performance pseudocapacitors. *J. Mater. Chem. A* **2017**, *5*, 1035–1042.
20. Hou, X.; Peng, T.; Cheng, J.; Yu, Q.; Luo, R.; Lu, Y.; Lu, Y.; Liu, X.; Kim, J.-K.; He, J.; et al. Ultrathin ZnS nanosheet/carbon nanotube hybrid electrode for high-performance flexible all-solid-state supercapacitor. *Nano Res.* **2017**, *10*, 2570–2583.
21. Li, G.-C.; Liu, M.; Wu, M.-K.; Liu, P.-F.; Zhou, Z.; Zhu, S.-R.; Liu, R.; Han, L. MOF-derived self-sacrificing route to hollow NiS<sub>2</sub>/ZnS nanospheres for high performance supercapacitors. *RSC Adv.* **2016**, *6*, 103517–103522.
22. Pei, L.; Yang, Y.; Chu, H.; Shen, J.; Ye, M. Self-assembled flower-like FeS<sub>2</sub>/graphene aerogel composite with enhanced electrochemical properties. *Ceram. Int.* **2016**, *42*, 5053–5061.
23. Acerce, M.; Voiry, D.; Chhowalla, M. Metallic 1T phase MoS<sub>2</sub> nanosheets as supercapacitor electrode materials. *Nat. Nanotechnol.* **2015**, *10*, 313–318.
24. Gigot, A.; Fontana, M.; Serrapede, M.; Castellino, M.; Bianco, S.; Armandi, M.; Bonelli, B.; Pirri, C.F.; Tresso, E.; Rivolo, P. Mixed 1T-2H Phase MoS<sub>2</sub>/Reduced Graphene Oxide as Active Electrode for Enhanced Supercapacitive Performance. *ACS Appl. Mater. Interfaces* **2016**, *8*, 32842–32852.
25. Yan, W.; Ayvazian, T.; Kim, J.; Liu, Y.; Donovan, K.C.; Xing, W.; Yang, Y.; Hemminger, J.C.; Penner, R.M. Mesoporous manganese oxide nanowires for high-capacity, high-rate, hybrid electrical energy storage. *ACS Nano* **2011**, *5*, 8275–8287.
26. Lee, H.Y.; Goodenough, J.B. Supercapacitor Behavior with KCl Electrolyte. *J. Solid State Chem.* **1999**, *144*, 220–223.
27. Kou, S.; Wu, N. Investigation of Pseudocapacitive Charge-Storage Reaction of MnO<sub>2</sub>·nH<sub>2</sub>O Supercapacitors in Aqueous Electrolytes. *J. Electrochem. Soc.* **2006**, *153*, A1317–A1324.
28. Broughton, J.N.; Brett, M.J. Variations in MnO<sub>2</sub> electrodeposition for electrochemical capacitors. *Electrochim. Acta* **2005**, *50*, 4814–4819.
29. Shinomiya, T.; Vinay, G.; Norio, M. Effects of electrochemical-deposition method and microstructure on the capacitive characteristics of nano-sized manganese oxide. *Electrochim. Acta* **2006**, *51*, 4412–4419.
30. Wu, M.-S. Electrochemical capacitance from manganese oxide nanowire structure synthesized by cyclic voltammetric electrodeposition. *Appl. Phys. Lett.* **2005**, *87*, 153102.
31. Chou, S.; Cheng, F.; Chen, J. Electrodeposition synthesis and electrochemical properties of nanostructured γ-MnO<sub>2</sub> films. *J. Power Source* **2006**, *162*, 727–734.
32. Hu, C.-C.; Tsou, T.-W. Ideal capacitive behavior of hydrous manganese oxide prepared by anodic deposition. *Electrochem. Commun.* **2002**, *4*, 105–109.
33. Zhai, T.; Xie, S.; Yu, M.; Fang, P.; Liang, C.; Lu, X.; Tong, Y. Oxygen vacancies enhancing capacitive properties of MnO<sub>2</sub> nanorods for wearable asymmetric supercapacitors. *Nano Energy* **2014**, *8*, 255–293.
34. Serrapede, M.; Rafique, A.; Fontana, M.; Zine, A.; Rivolo, P.; Bianco, S.; Chetibi, L.; Tresso, E.; Lamberti, A. Fiber-shaped asymmetric supercapacitor exploiting rGO/Fe<sub>2</sub>O<sub>3</sub> aerogel and electrodeposited MnO<sub>x</sub> nanosheets on carbon fibers. *Carbon* **2019**, *144*, 91–100.
35. Rafique, A.; Massa, A.; Fontana, M.; Bianco, S.; Chiodoni, A.; Pirri, C.F.; Hernández, S.; Lamberti, A. Highly Uniform Anodically Deposited Film of MnO<sub>2</sub> Nanoflakes on Carbon Fibers for Flexible and Wearable Fiber-Shaped Supercapacitors. *ACS Appl. Mater. Interfaces* **2017**, *9*, 28386–28393.
36. Ramírez, A.; Hillebrand, P.; Stellmach, D.; May, M.M.; Bogdanoff, P.; Fiechter, S. Evaluation of MnO<sub>x</sub>, Mn<sub>2</sub>O<sub>3</sub>, and Mn<sub>3</sub>O<sub>4</sub> Electrodeposited Films for the Oxygen Evolution Reaction of Water. *J. Phys. Chem. C* **2014**, *118*, 14073–14083.
37. Ilton, E.S.; Post, J.E.; Heaney, P.J.; Ling, F.T.; Kerisit, S.N. XPS determination of Mn oxidation states in Mn (hydr)oxides. *Appl. Surf. Sci.* **2016**, *366*, 475–485.
38. Ardizzione, S.; Bianchi, C.L.; Tirelli, D. Mn<sub>3</sub>O<sub>4</sub> and γ-MnOOH powders, preparation, phase composition and XPS characterisation. *Colloid Surf. A Physicochem. Eng. Asp.* **1998**, *134*, 305–312.



39. Nesbitt, H.W.; Banerjee, D. Interpretation of XPS Mn(2p) spectra of Mn oxyhydroxides and constraints on the mechanism of MnO<sub>2</sub> precipitation. *Am. Mineral.* **1998**, *83*, 305–315.
40. Biesinger, M.C.; Payne, B.P.; Grosvenor, A.P.; Lau, L.W.; Gerson, A.R.; Smart, R.S.C. Resolving surface chemical states in XPS analysis of first row transition metals, oxides and hydroxides: Cr, Mn, Fe, Co and Ni. *Appl. Surf. Sci.* **2011**, *257*, 2717–2730.
41. Chiodoni, A.; Salvador, G.P.; Massaglia, G.; Delmondo, L.; Munoz-Tabares, J.A.; Sacco, A.; Garino, N.; Castellino, M.; Ahmed, M.D.; Pirri, C.F.; et al. Mn<sub>x</sub>O<sub>y</sub>- based cathodes for oxygen reduction reaction catalysis in microbial fuel cells. *Int. J. Hydrog. Energy* **2019**, *44*, 4432–4441.
42. Mayorga-Martinez, C.C.; Ambrosi, A.; Eng, A.Y.S.; Sofer, Z.; Pumera, M. Transition metal dichalcogenides (MoS<sub>2</sub>, MoSe<sub>2</sub>, WS<sub>2</sub> and WSe<sub>2</sub>) exfoliation technique has strong influence upon their capacitance. *Electrochem. Commun.* **2015**, *56*, 24–28.
43. Karade, S.S.; Dubal, D.P.; Sankapal, B.R. MoS<sub>2</sub> ultrathin nanoflakes for high performance supercapacitors: Room temperature chemical bath deposition (CBD). *RSC Adv.* **2016**, *6*, 39159–39165.
44. Cai, L.; He, J.; Liu, Q.; Yao, T.; Chen, L.; Yan, W.; Hu, F.; Jiang, Y.; Zhao, Y.; Hu, T.; et al. Vacancy-Induced Ferromagnetism of MoS<sub>2</sub> Nanosheets. *J. Am. Chem. Soc.* **2015**, *137*, 2622–2627.
45. Voiry, D.; Salehi, M.; Silva, R.; Fujita, T.; Chen, M.; Asefa, T.; Shenoy, V.B.; Eda, G.; Chhowalla, M. Conducting MoS<sub>2</sub> nanosheets as catalysts for hydrogen evolution reaction. *Nano Lett.* **2013**, *13*, 6222–6227.
46. Liu, T.-C.; Pell, W.G.; Conway, B.E.; Roberson, S.L. Behavior of Molybdenum Nitrides as Materials for Electrochemical Capacitors. *J. Electrochem. Soc.* **1998**, *145*, 6.
47. Toupin, M.; Brousse, T.; Belanger, D. Charge storage mechanism of MnO<sub>2</sub> electrode used in aqueous electrochemical capacitor. *Chem. Mater.* **2004**, *15*, 3184–3190.
48. Wei, W.; Cui, X.; Chen, W.; Ivey, D.G. Manganese oxide-based materials as electrochemical supercapacitor electrodes. *Chem. Soc. Rev.* **2011**, *40*, 1697–1721.
49. Murali, S.; Quarles, N.; Zhang, L. L.; Potts, J. R.; Tan, Z.; Lu, Y.; Zhu, Y.; Ruoff, R. S. Volumetric capacitance of compressed activated microwave-expanded graphite oxide (a-MEGO) electrodes. *Nano Energy* **2013**, *2*, 764–768.
50. Lukatskaya, M.R.; Mashtalir, O.; Ren, C. E.; Dall’Agnese, Y.; Rozier, P.; Taberna, P. L.; Naguib, M.; Simon, P.; Barsoum, M.W.; Gogotsi, Y. Cation intercalation and high volumetric capacitance of two-dimensional titanium carbide. *Nanoscale* **2015**, *7*, 1502–1505.
51. Brusse, T.; Toupin, M.; Dugas, R.; Athouël, L.; Crosnier, O.; Bélanger, D. Crystalline MnO<sub>2</sub> as Possible Alternatives to Amorphous Compounds in Electrochemical Supercapacitors. *J. Electrochem. Soc.* **2006**, *153*, A2171–A2180.
52. Ghodbane, O.; Pascal, J.-L.; Favier, F. Microstructural effects on charge-storage properties in MnO<sub>2</sub>-based electrochemical supercapacitors. *ACS Appl. Mater. Interfaces* **2009**, *1*, 1130–1139.
53. Camacho, R.A.P.; Wu, A. M.; Gao, S.; Jin, X.-Z.; Cao, G.-Z.; Huang, H. Mn<sub>3</sub>O<sub>4</sub> nanoparticles encapsulated in carbon cages as the electrode of dual-mechanism supercapacitors. *Mater. Chem.* **2019**, *12*, 361–372.
54. Toupin, M.; Brousse, T.; Belanger, D. Influence of Microstructure on the Charge Storage Properties of Chemically Synthesized Manganese Dioxide. *Chem. Mater.* **2002**, *14*, 3946–3952.
55. Brezesinski, K.; Wang, J.; Haetge, J.; Reitz, C.; Steinmueller, S. O.; Tolbert, S. H.; Smarsly, B.M.; Dunn, B.; Brezesinski, T. Pseudocapacitive contributions to charge storage in highly ordered mesoporous group v transition metal oxides with iso-oriented layered nanocrystalline domains. *J. Am. Chem. Soc.* **2010**, *132*, 6982–6990.
56. Soon, J.M.; Loh, K.P. Electrochemical Double-Layer Capacitance of MoS<sub>2</sub> Nanowall Films. *Electrochem. Solid State Lett.* **2007**, *10*, A250–A254.
57. Rowly-Neal, S.J.; Brownson, D. A.; Smith, G. C.; Sawtell, D. A.; Kelly, P. J.; Banks, C. E. 2D nanosheet molybdenum disulphide (MoS<sub>2</sub>) modified electrodes explored towards the hydrogen evolution reaction. *Nanoscale* **2015**, *7*, 18152–18168.
58. Zhu, H.; Lyu, F.; Du, M.; Zhang, M.; Wang, Q.; Yao, J.; Guo, B. Design of two-dimensional, ultrathin MoS<sub>2</sub> nanoplates fabricated within one-dimensional carbon nanofibers with thermosensitive morphology: High-performance electrocatalysts for the hydrogen evolution reaction. *ACS Appl. Mater. Interfaces* **2014**, *6*, 22126–22137.
59. Li, G.; Zhang, Y.; Huang, S.; Yang, W.; Cao, L. Activating MoS<sub>2</sub> for pH-Universal Hydrogen Evolution Catalysis. *J. Am. Chem. Soc.* **2017**, *139*, 16194–16200.

60. Zhang, B.; Ji, X.; Xu, K.; Chen, C.; Xiong, X.; Xiong, J.; Yao, Y.; Miao, L.; Jiang, J. Unraveling the different charge storage mechanism in T and H phases of MoS<sub>2</sub>. *Electrochem. Acta* **2016**, *217*, 1–8.
61. Dupont, M.; Donne, S. W. Separating Faradaic and Non-Faradaic Charge Storage Contributions in Activated Carbon Electrochemical Capacitors Using Electrochemical Methods: I. Step Potential Electrochemical Spectroscopy. *J. Electrochem. Soc.* **2015**, *162*, A1246–A1254.
62. Yang, X.; Niu, H.; Jiang, H.; Wang, Q.; Qu, F. A high energy density all-solid-state asymmetric supercapacitor based on MoS<sub>2</sub>/graphene nanosheets and MnO<sub>2</sub>/graphene hybrid electrodes. *J. Mater. Chem. A* **2016**, *4*, 11264.
63. Javed, M.S.; Dai, S.; Wang, M.; Guo, D.; Chen, L.; Wang, X.; Hu, C.; Xi, Y. High performance solid state flexible supercapacitor based on molybdenum sulfide hierarchical nanospheres. *J. Power Source* **2015**, *285*, 63–69.
64. Zhao, C.; Zhou, Y.; Ge, Z.; Zhao, C.; Qian, X. Facile construction of MoS<sub>2</sub>/RCF electrode for high-performance supercapacitor. *Carbon* **2018**, *127*, 699–706.
65. Zhou, C.; Wang, J.; Yan, X.; Yuan, X.; Wang, D.; Zhu, Y.; Cheng, X. Vertical MoS<sub>2</sub> nanosheets arrays on carbon cloth as binder-free and flexible electrode for high-performance all-solid-state symmetric supercapacitor. *Ceram. Int.* **2019**, *45*, 21534–21543.
66. Sun, P.; Wang, R.; Qiang, W.; Wang, H.; Wang, X. Uniform MoS<sub>2</sub> nanolayer with sulfur vacancy on carbon nanotube networks as binder-free electrodes for asymmetrical supercapacitor. *Appl. Surf. Sci.* **2019**, *475*, 793–802.
67. Xue, T.; Yang, Y.; Yan, X.-H.; Zou, Z.-L.; Han, F.; Yang, Z. Free standing and binder free Molybdenumbisulfide nanospheres/reduced graphene oxide composite paper as flexible electrode for symmetric supercapacitor. *Mater. Res. Express* **2019**, *6*, 095029.
68. Wang, X.; Ding, W.; Li, H.; Li, H.; Zhu, S.; Zhu, X.; Sun, Y.; Dou, S.X. Unveiling highly ambient-stable multilayered 1T- MoS<sub>2</sub> towards all-solid-state flexible supercapacitors. *J. Mater. Chem. A* **2019**, *7*, 19152.
69. Zhao, Y.; He, X.; Chen, R.; Liu, Q.; Liu, J.; Yu, J.; Zhang, H.; Dong, H.; Zhang, M.; Li, R.; Wang, J. Flexible all-solid-state asymmetric supercapacitor based on three-dimensional MoS<sub>2</sub>/Ketjen black nanoflower arrays. *Int. J. Hydrog. Energy* **2019**, *44*, 13690–13699.
70. He, J.; Yang, D.; Li, H.; Cao, X.; Kang, L.; He, X.; Jiang, R.; Sun, J.; Lei, Z.; Liu, Z.-H.. Mn<sub>3</sub>O<sub>4</sub>/RGO/SWCNT hybrid film for all-solid-state flexible supercapacitor with high energy density. *Electrochim. Acta* **2018**, *283*, 174–182.
71. Arul, N.S.; Han, J.; Chen, P.C. Solid State Supercapacitor Based on Manganese Oxide@Reduced Graphene Oxide and Polypyrrole Electrodes. *ChemElectroChem* **2018**, *5*, 2747–2757.
72. Aswathy, R.; Ulaganathan, M.; Rugupathy, P. Mn<sub>3</sub>O<sub>4</sub> nanoparticles grown on surface activated graphite paper for aqueous asymmetric supercapacitors. *J. Alloy Compd.* **2018**, *767*, 141–150.
73. Beyazay, T.; Oztuna, F.E.S.; Unal, U. Self-Standing Reduced Graphene Oxide Papers Electrodeposited with Manganese Oxide Nanostructures as Electrodes for Electrochemical Capacitors. *Electrochim. Acta* **2019**, *296*, 916–924.
74. Jian, H.; Zhang, Y.; Wang, C.; Wang, Q.; Meng, C.; Wang, J. Rice husk-derived Mn<sub>3</sub>O<sub>4</sub>/manganese silicate/C nanostructured composites for high-performance hybrid supercapacitors. *Inorg. Chem. Front.* **2019**, *6*, 2788.
75. Fan, L.; Zhang, Y.; Guo, Z.; Sun, B.; Tian, D.; Feng, Y.; Zhang, N.; Sun, K. Hierarchical Mn<sub>3</sub>O<sub>4</sub> Anchored on 3D Graphene Aerogels via C-O-Mn Linkage with Superior Electrochemical Performance for Flexible Asymmetric Supercapacitor. *Chem. Eur. J.* **2019**, *25*, 1–6.
76. Yu, N.; Yin, H.; Zhang, W.; Liu, Y.; Tang, Z.; Zhu, M. Q. High-Performance Fiber-Shaped All-Solid-State Asymmetric Supercapacitors Based on Ultrathin MnO<sub>2</sub> Nanosheet/Carbon Fiber Cathodes for Wearable Electronics. *Adv. Energy Mater.* **2016**, *6*, 1501458.
77. Zhao, C.; Ge, Z.; Zhou, Y.; Huang, Y.; Wang, G.; Qian, X. Solar-assisting pyrolytically reclaimed carbon fiber and their hybrids of MnO<sub>2</sub>/RCF for supercapacitor electrodes. *Carbon* **2017**, *114*, 230–241.

